Energy & Environmental Science

ROYAL SOCIETY OF CHEMISTRY

PAPER

View Article Online
View Journal

Cite this: DOI: 10.1039/d6ee00064a

Tailoring an iron-based metal–organic framework for a Zn-ORR/CER battery

Sukhjot Kaur,[a] Safa Gaber,[b] Kalpana Garg,[a] Abdul Khayum Mohammed,[b] Ankur Bordoloi,[c] Harpriya Minhas,[d] Biswarup Pathak,[d] Dinesh Shetty *[be] and Tharamani C. Nagaiah *[a]

Received 5th January 2026,
Accepted 1st May 2026

DOI: 10.1039/d6ee00064a

rsc.li/ees

Chlorine (Cl_2) is a vital industrial product obtained from waste. Replacing the non-sustainable industrial synthesis of Cl_2 with the electrochemical conversion of HCl provides a greener alternative. Moreover, integrating Cl_2 synthesis with Zn-based batteries helps to meet growing energy demands. Herein, we coupled the oxygen reduction reaction (ORR) during discharge and the chlorine evolution reaction (CER) during charge to develop a Zn-ORR/CER battery that utilizes an Fe-based metal organic framework (Fe-Tp) as a robust bifunctional electrocatalyst. This approach facilitates a *'hitting three targets with one shot'* strategy *viz.* waste remediation, production of value-added Cl_2, and energy storage and conversion. Apart from providing stable battery performance under corrosive reaction conditions, this report provides an analysis of catalyst renewal during the CER *via* spectro-electrochemical studies. Moreover, the local pH changes were taken into consideration through detailed microelectrochemical analysis. The assembled battery has fast-charging capability, as demonstrated by powering 35 LEDs for 8 h after 10 minutes of charging, making this a viable battery.

Broader context

Chlorine (Cl_2) is an indispensable industrial chemical underpinning the production of polymers, pharmaceuticals and agrochemicals. However, its conventional manufacture *via* chlor-alkali or HCl electrolysis remains highly energy-intensive and is burdened by safety risks arising from the concurrent hydrogen evolution reaction (HER) and Cl_2 accumulation. Therefore, there is an urgent need to redesign Cl_2 production routes that simultaneously reduce energy consumption, mitigate safety hazards and enable energy recovery. Therefore, in the present work, we have replaced the HER (E^0 = 0 V *vs.* NHE) with the oxygen reduction reaction (ORR, E^0 = 1.23 V *vs.* NHE), which significantly reduces the overall voltage to −0.13 V (CER-ORR) compared to the CER-HER (−1.36 V) system. However, the practical implementation of this approach has traditionally been limited by the lack of cost-effective, corrosion-resistant, and bifunctional electrocatalysts capable of operating under strongly acidic conditions. Further, integrating such reactions with energy-storage systems remains largely unexplored. This work establishes a new paradigm by unifying Cl_2 production with electrochemical energy storage through an aqueous Zn-ORR/CER battery enabled by a non-noble, iron-based metal–organic framework cathode. By simultaneously generating Cl_2 and electricity with long-term stability, this approach transforms hazardous chemical synthesis into an energy-positive process. Beyond Cl_2 chemistry, the concept demonstrates how industrial redox reactions can be rationally coupled with battery architectures to create safer, more efficient and sustainable electrochemical manufacturing platforms, paving the way for future electrified chemical processes.

Introduction

Increasing energy demands and the pressure of environmental issues have increased the emphasis on sustainable development research areas, ranging from water-splitting electrolyzers to metal–air batteries.[1] Although these systems represent promising ways to store energy without any carbon emissions, the oxygen evolution reaction (OER) provides sluggish kinetics and hinders the overall reaction thermodynamics. Therefore, various small molecules have been investigated to replace the OER.[2,3] One such molecule is hydrochloric acid (HCl), as it is produced and discarded as waste in industrial processes such

[a] Department of Chemistry, Indian Institute of Technology Ropar, Rupnagar, Punjab, India. E-mail: tharamani@iitrpr.ac.in
[b] Department of Chemistry, Khalifa University of Science & Technology, Abu Dhabi, P.O. Box 127788, United Arab Emirates. E-mail: dinesh.shetty@ku.ac.ae
[c] Nanocatalysis (LSP Division), CSIR-Indian Institute of Petroleum, Dehradun, Uttarakhand, 248005, India
[d] Department of Chemistry, Indian Institute of Technology (IIT) Indore, Indore, Madhya Pradesh, 453552, India
[e] Center for Catalysis & Separations (CeCaS), Khalifa University of Science & Technology, Abu Dhabi, P.O. Box 127788, United Arab Emirates

as chlorine (Cl_2) production, steel and metal finishing, pickling and cleaning. Conversion of this waste HCl into value-added products *via* a recycling process to produce Cl_2 could be a game-changing strategy.[4] Cl_2 is an important industrial chemical used in the production of polymers, resins, water disinfectants and in smart and advanced technologies.[5–8] The increasing demand for Cl_2 is causing its market size to rise at a compound annual growth rate of $>3.5\%$, meaning it is projected to reach 67.2 billion dollars by 2032.[9,10] However, the Cl_2 is industrially produced *via* the Deacon process or the chlor-alkali process, which are inefficient due to their high catalyst demand, poor catalyst stability, and the fact that they consume 4% of global electricity. Of late, Cl_2 production *via* electrocatalytic oxidation of HCl using ruthenium-based catalysts has emerged as a promising technology (eqn (1)–(3)).[11] However, the major drawbacks of this technology are the requirement of high cell potential (1.36 V, eqn (3)) and high electricity consumption. In fact, the $\sim$1500 kWh per metric per ton of Cl_2 required accounts for around 50% of the production costs, which is still 3.5 times lower compared to the chlor-alkali process. Although this process is relatively energy efficient, it suffers from critical safety concerns related to the accumulation of the produced H_2 and Cl_2 at the cathode during uncontrolled shutdown. Therefore, replacing the hydrogen evolution reaction (HER, E^0 = 0 V *vs.* NHE) with the oxygen reduction reaction (ORR, E^0 = 1.23 V *vs.* NHE) reduces the overall cell voltage to -0.13 V (CER-ORR) when compared to the CER-HER system (-1.36 V).[12–16]

$$\text{Cathode: } 2H^+ + 2e^- \rightarrow H_{2(g)} \quad E = 0.00 \text{ V } \textit{vs.} \text{ NHE} \tag{1}$$

$$\text{Anode: } 2Cl^- \rightarrow Cl_{2(g)} + 2e^- \quad E = 1.36 \text{ V } \textit{vs.} \text{ NHE} \tag{2}$$

$$\text{Overall: } 2HCl \rightarrow H_{2(g)} + Cl_{2(g)} \quad E = -1.36 \text{ V } \textit{vs.} \text{ NHE} \tag{3}$$

More importantly, the electrolysis of HCl requires an external electron source. Notably, integrating this system with aqueous rechargeable Zn-based batteries[17–22] could prove to be beneficial by "*hitting three targets with one shot*" *viz.*, waste utilization and Cl_2 production along with energy storage and conversion. In the resultant Zn-ORR/CER battery, during discharging, the oxygen reduction reaction takes place, which facilitates Zn oxidation at the anode; whereas during the charging process, chlorine evolution reaction is facilitated by the reduction of Zn^{2+} to Zn (eqn (4)–(7)).

Discharge process:

$$\text{Cathode: } O_2 + 4H^+ + 4e^- \rightarrow H_2O \tag{4}$$

$$\text{Anode: } Zn \leftrightarrows Zn^{2+} + 2e^- \tag{5}$$

$$Zn^{2+} + 4OH^- \leftrightarrows Zn(OH)_4^{2-}$$

$$Zn(OH)_4^{2-} \leftrightarrows ZnO + H_2O + 2OH^-$$

Charging process:

$$\text{Cathode: } 2HCl \leftrightarrows Cl_2 + 2H^+ + 2e^- \tag{6}$$

$$\text{Anode: } Zn(OH)_4^{2-} \leftrightarrows Zn^{2+} + 4OH^- \tag{7}$$

$$Zn^{2+} + 2e^- \leftrightarrows Zn$$

However, electrochemical Cl_2 production coupled with an oxygen depolarized cathode (ODC)[17,19,23–25] requires the design of a robust bifunctional electrocatalyst that can tolerate a corrosive HCl environment, be economically scalable, and can also perform stably in industry upon sudden shutdown. For example, Pt/C is a state-of-the-art catalyst for the electrochemical ORR reaction, but it is unstable in HCl media. Meanwhile, only a handful of catalysts have been studied so far for both the CER and ORR reactions, such as Rh-RhS_x/CNT,[26] Pt-Ag,[27] and non-noble metal catalysts such as vacancy-rich $Ni_{2-x}P$,[28] Co-NSC,[29] OCNT-PVIM-ZnPOM,[30] Cu-Fe_2O_3/NC,[31] and covalent organic frameworks such as Tta-Dfp and Tab-Dfp.[32] For an efficient functioning of the Zn-ORR/CER battery, the electrocatalyst must be bifunctionally active for both the discharging and charging reactions. This requires a material with sufficient adsorption sites for the chloride ions and oxygen during charge-discharge cycles, and it should exhibit porosity and conductivity to facilitate mass diffusion and electron mobility. So far, only one report on a Zn-ORR/CER battery exists, which is based on an Ag catalyst,[33] but the high cost of silver hinders its large-scale implementation. To be competitive in the mainstream commercial market, non-noble catalysts that are both low-cost and abundant are the need of the hour.

Keeping this in mind, we have introduced an iron (Fe)-coordinated salicylaldehydate-based three-dimensional conjugated metal–organic framework (Fe-Tp) as a bifunctional catalyst for a Zn-ORR/CER battery. Metal–organic frameworks (MOFs) are crystalline porous solids connected *via* coordination bonds between metal ions/clusters and organic linkers.[34] The strong π-d conjugated coordination in Fe-Tp provides a robust framework with uniformly distributed iron atoms and ensures electronic conductivity. Moreover, Fe is a low-cost and widely available metal, offering a cost-effective and scalable alternative to noble metal-based catalysts. During oxidation, Fe-Tp adsorbs chlorine, and during reduction, it adsorbs oxygen through its redox-active functional network. Moreover, the strong coordination bonds render Fe-Tp chemical stability within the system, which supports long-term performance. Also, triformylphloroglucinol (Tp)-based covalent organic frameworks have been reported to provide a well-defined and rigid coordination environment for CER, wherein they show efficient Cl* adsorption under industrially relevant Cl^- ion concentrations.[35] Moreover, Fe-based catalysts have been shown to favor the ORR owing to their strong hybridization between the Fe 3d orbitals and O_2 π orbitals.[36] Moreover, Fe^{3+} shows a strong Lewis acid–base interaction with O_2 molecules, enabling its facile adsorption and conversion.

In an acidic medium, the coordination environment of the Fe^{2+}/Fe^{3+} ions promotes the protonation of *OOH intermediates. The abundant H^+ ions in such conditions facilitate proton transfer from the Fe^{2+}/Fe^{3+} to *OOH, resulting in the formation of *OH species. Subsequent desorption of *OH produces H_2O. Additionally, the interaction between the Fe^{2+}/Fe^{3+} ions and the oxygen atoms of the ligands lowers the electron-transfer resistance, thereby enhancing the transfer of electrons from the oxygen molecules to the catalytically active sites during the ORR process.[37]

In addition, we have designed a hybrid of Fe-Tp with graphene (G) layers (Fe-Tp-*x*%G), which enhances the overall dispersion of Fe-Tp as a catalyst in the system and further improves the electrical conductivity. For the CER process, as depicted in the theoretical studies, *OCl adsorption is more favorable at the Fe-Tp units, and graphene shows stronger interactions with *Cl and thus, Fe-Tp-G shows moderated adsorption of *Cl with balanced Bader charges to enhance CER activity. The designed Fe-Tp-10% G bifunctional cathode for the Zn-ORR/CER battery was demonstrated by glowing 35 LEDs for 8 h after only 10 min of charge. Moreover, the electrochromic effect and local pH studies have been utilized for the CER in 0.4 M HCl, which remain unexplored for this application.

Results and discussion

Synthesis and characterization

Fe-Tp-*x*%G was synthesized *via* an *in situ* inclusion of graphene layers (*x*%: 5 to 15 wt% of the monomers) during the mechanochemical mixing of the organic linker (Tp: 1,3,5-triformylphloroglucinol) and $FeCl_3{\cdot}6H_2O$. The mixture was thermally treated at 90 °C for 24 hours in a closed container (Fig. 1a). The resulting solid monoliths were washed using various solvents (*N*,*N*-dimethylacetamide, water, and acetone) to remove unreacted reagents to obtain a dark brown powder (detailed in SI). Notably, the powder X-ray diffraction (PXRD) pattern showed the presence of Fe-Tp MOF and graphene layers with their characteristic peaks. The sharp crystalline peaks at 2θ values of ~17.2°, 18.4°, and 18.8° indicated the formation of biphasic crystalline Fe-Tp (Fig. 1b), which is similar to our previously reported pristine MOF.[38,39] In addition, the presence of a peak at 2θ = 26.7° (002) validates the presence of graphene in the synthesised Fe-Tp-*x*% G (Fig. 1b and Fig. S1).

Furthermore, the FT-IR spectrum exhibits new peaks at around 1558 cm^{-1}, 1477 cm^{-1}, and 1240 cm^{-1}, indicating the formation of C=O, C=C, and C–O coordination bonds, respectively. (Fig. S2).[38,39] The N_2 gas adsorption analysis highlighted the porous features of Fe-Tp within the mixture with a Brunauer–Emmett–Teller (BET) surface area of 112 $m^2\ g^{-1}$ (Fig. S3).[38,39] The

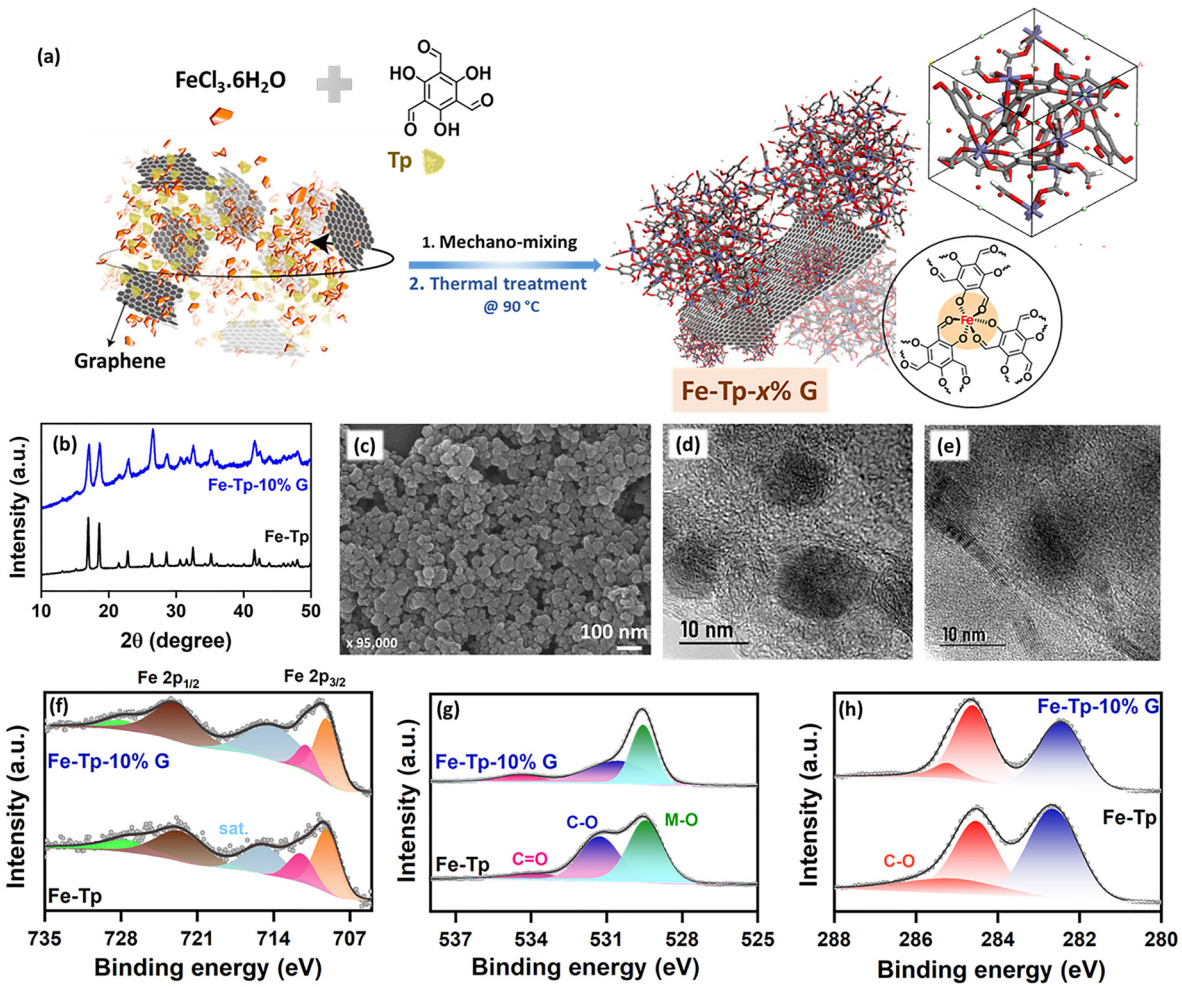

Fig. 1 (a) Schematic representation of the synthesis of FeTp-*x*% G showing the theoretical model of Fe-Tp, (b) the P-XRD patterns of pristine Fe-Tp and the Fe-Tp-10% G, (c) the FE-SEM image of Fe-Tp-10% G, (d) and (e) the TEM images of Fe-Tp-10% G, and the deconvoluted (f) Fe 2p, (g) O 1s and (h) C 1s XPS spectra for both Fe-Tp and Fe-Tp-10% G.

morphological attributes of the designed catalyst were examined using field-emission scanning electron microscopy (FE-SEM), which revealed the formation of spheres in Fe-Tp-10% G (Fig. 1c). This was also further supported by the transmission electron microscopy (TEM) images of Fe-Tp-10% G (Fig. 1d, e and Fig. S4).

Notably, the HR-TEM images revealed the nanoscopic assembly of Fe-Tp over the surface of the graphene layers (Fig. 1e). Moreover, TEM-energy dispersive X-ray spectroscopic (EDS) analysis showed the homogenous distribution of Fe, C and O in both Fe-Tp and Fe-Tp-10% G (Fig. S5–S7). The selected area electron diffraction (SAED) pattern of Fe-Tp-10% G shows the presence of diffuse rings along with bright spots (Fig. S8) confirming its crystallinity. The electronic structures of both Fe-Tp and the Fe-Tp-*x*% G variants were analysed using X-ray photoelectron spectroscopy (XPS), wherein the XPS survey scan revealed a similar XPS spectra for all the variants with C, O and Fe elements present in it with no impurities from the reaction mixture (Fig. S9). Further, the Fe 2p XPS spectra were deconvoluted into two spin–orbit doublets at bindings corresponding to $2p_{1/2}$ and $2p_{3/2}$ (Fig. 1f) along with a satellite peak at 715.15 eV. The O1s XPS spectra were deconvoluted into three peaks at B.E. of 529.46 eV, 531.30 eV and 534.37 eV, attributed to M-O, C–O (phenolic O) and C═O (aldehydic O), respectively (Fig. 1g). Similarly, the C1s XPS spectra were deconvoluted into 3 peaks at B.E. of 282.6 eV, 284.5 eV and 285.23 eV, respectively (Fig. 1h). Furthermore, since the electrocatalytic activity of Fe-Tp-10% G was tested in acidic media (0.4 M HCl), it's stability was evaluated in the same environment by dispersing the powder in 0.4 M HCl solution for 24 h. Following this period, FE-SEM, TEM and P-XRD analyses were performed after thorough washing and drying. As illustrated in Fig. S10, the XRD, FE-SEM and TEM analyses reveal no significant changes in the microstructure and morphology, indicating that the catalyst did not dissolve in the solution.

Electrochemical chlorine evolution reaction

The efficacy of the designed catalyst (Fe-Tp and variants of Fe-Tp-*x*% G) for Cl_2 production was evaluated by various electrochemical techniques. Initially, linear sweep voltammetry (LSV) experiments were performed in 0.4 M HCl in the potential range from 1.0 V to 2.0 V *vs.* RHE at a scan rate of 5 mV s^{-1} while constantly stirring the solution at 600 rpm to facilitate the removal of bubbles from the electrode surface. As observed from the LSV curves in Fig. 2a (inset), the current density started to rise steeply at around 1.4 V for all the catalysts. Specifically, a current density of 100 mA cm^{-2} was achieved at 1.76 V for Fe-Tp-10% G, whereas a higher potential (Table S1) was required for Fe-Tp and other variants to reach the same current density.

To understand the interference from other electrochemical reactions *viz.*, the OER, the LSV curves were recorded in a Cl^--free electrolyte *i.e.*, 0.2 M H_2SO_4 (Fig. 2a). A comparison shows that the Fe-Tp-10% G requires a 1.78 V potential to reach a current density of 10 mA cm^{-2} in the Cl^--free electrolyte, while 1.46 V is required to reach the same current density in the presence of a Cl^--containing electrolyte, *i.e.*, OER being 320 mV higher than CER. Moreover, Fe-Tp-10% G reached a remarkable current density of 254.8 mA cm^{-2} at 2.0 V (Table S1), putting forth its superior activity for Cl_2 production, and is comparable

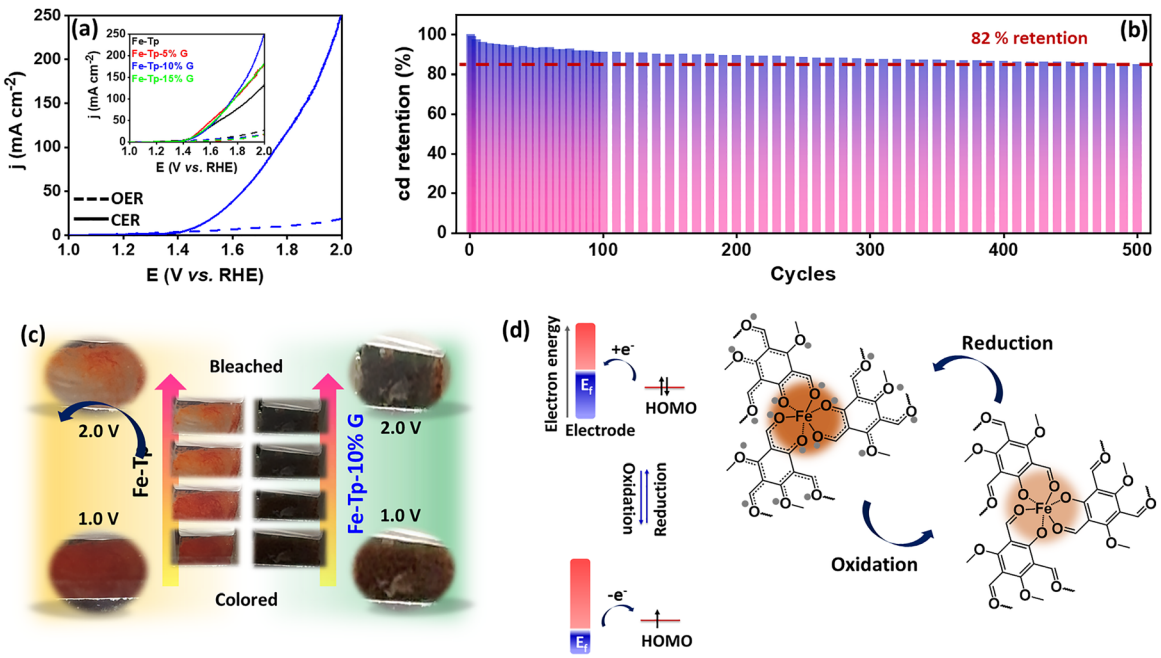

Fig. 2 (a) LSV curves for Fe-Tp-10% G in 0.4 M HCl (for the CER) and 0.2 M H_2SO_4 (for the OER) at a scan rate of 5 mV s^{-1} (inset, LSV curves of Fe-Tp and the Fe-Tp-*x*% G variants), (b) bar diagram showing current density retention up to 500 LSV cycles, (c) photographic images of the electrochromic effect on Fe-Tp and Fe-Tp-10% G represented by a color change, and (d) the mechanism of the electrochromic effect.

to those reported in the literature (Table S2). Also, a comparison of CER activity of Fe-Tp-10% G was carried out with that of only graphene to understand the intrinsic role of Fe-Tp MOF. As shown in Fig. S11 and Table S1, the graphene-only catalyst exhibits a lower current density and a higher potential (2.0 V) at 100 mA cm^{-2}. Furthermore, a careful examination of Fe-Tp-10% G towards CER activity was done by employing sequential chronoamperometry analyses (Fig. S12) at different potentials ranging from 0.8 V to 2.0 V. After observing a negligible rise in current density up to 1.3 V, a sudden rise was observed at 1.4 V, manifesting that the CER started between 1.3–1.4 V. Similarly, for the OER, a rise in current density was observed only after 1.8 V. The higher selectivity for CER in the HCl medium could be attributed to the faster kinetics for CER, as affirmed by the lower Tafel slope (135 mV dec^{-1}) for the CER as compared to the OER (367 mV dec^{-1}, Fig. S13).

The amount of Cl_2 gas produced during the CER was quantified for Fe-Tp, Fe-Tp-10% G, and pristine graphene *via* the iodometric titration method. To do this, chronoamperometric measurements were performed at 1.5 V for 10 min for each catalyst, and the chlorine generated during electrochemical reaction was quantified using iodometry (detailed in the SI), which revealed that Fe-Tp-10% G generated Cl_2 with a F.E. of ~96.5%, surpassing both Fe-Tp (87%) and graphene (78%, Table S3). To understand the stability of the designed Fe-Tp-10% G catalyst in Cl^--containing electrolytes, cycling experiments were performed up to 500 LSV cycles in 0.4 M HCl (Fig. S14). As observed from the LSV curves in Fig. S14, no changes in the potential were observed; however, an 18% decrease in the current density was observed after 500 cycles (Fig. 2b). For a similar reason, chronoamperometry was performed at 1.5 V *vs.* RHE for 12 h (Fig. S15) and an average current density of ~29.4 mA cm^{-2} was obtained, which was stable for 12 h, depicting the robustness of the catalyst in the presence of Cl^- ions. More importantly, the activity of Fe-Tp-10% G was investigated in highly corrosive conditions (Cl^--rich electrolyte *i.e.*, 5 M HCl) and a current density of 416.82 mA cm^{-2} was achieved at 1.8 V *vs.* RHE (Fig. S16).

Additionally, to investigate whether any Fe leaches from the framework during electrolysis, the electrolyte following the stability studies was examined *via* Microwave Plasma Atomic Emission Spectrometry (MPAES). The concentration of Fe^{3+} in the solution was recorded from MPAES before the reaction and after 1 h and 24 h of the CER using the calibration curve (Fig. S17, detailed in the SI). As shown in Table S4, there is negligible dissolution of Fe in the solution, signifying the stability of the catalyst in solution. This was further confirmed *via* fast scanning electrochemical experiments carried out using a homemade carbon microelectrode as the WE, Pt wire as the CE and Ag/AgCl/3 M KCl as the RE. Being highly sensitive, the microelectrode was chosen to detect any trace amounts of metal species, *viz.* Fe^{2+}/Fe^{3+}, in the electrolyte, which could be leached out in the solution after the CER. At first, known amounts of $FeCl_3$ (5 and 8 ppm) were added into 0.4 M HCl and cyclic voltammetry (CV) was conducted at different scan rates (50 mV s^{-1} to 1 V s^{-1}). The obtained CV curves showed characteristic redox peaks of Fe^{2+}/Fe^{3+}, as shown in Fig. S18. Subsequently, the electrolyte solution obtained following chronoamperometry for 1 h was analyzed for any Fe metal species. As illustrated in the lower section of Fig. S18, a small redox peak corresponding to Fe was detected, which could also be seen through the MPAES analysis.

Electrochromic effect

The electrochromic effect was also studied to deduce the changes on the electrode surface during the CER using UV-Vis spectrophotometry. For this purpose, the electrocatalyst (Fe-Tp or Fe-Tp-10% G) was coated on a fluorine-doped tin oxide (FTO) surface, which served as the working electrode (WE), whilst Ag/AgCl/3 M KCl and a graphite rod were used as the reference and counter electrodes, respectively. The UV-Vis spectra and the simultaneous change in the color on the WE during the electrochromic test were obtained using an *in situ* UV-Vis spectro-electrochemical setup (detailed in the SI). The visualization studies show noticeable changes in the color on the WE, clearly as the potential was swept from 1.0 to 2.2 V. The initial red color of the Fe-Tp gradually changed to transparent (Fig. 2c and Fig. S19), while for Fe-Tp-10% G, the color changes from brown (initial) to black (Fig. 2c and Fig. S20 and Movie S1, SI). In both the catalysts, Fe-Tp gradually changed color and eventually became colorless. This change suggests the transformation of the O-containing moieties from C–OH groups coordinated to the Fe metal centre (red color) to C═O species (pale yellow color, Fig. 2d), indicating H-atom abstraction (ligand dehydrogenation[35]). This transformation leads to a metal-to-ligand charge transfer absorption, as observed in the UV-Vis spectra (~600 nm, Fig. S21). Also, it is known that in the presence of UV light, switching between Fe^{2+} and Fe^{3+} can occur, resulting in a Fenton-like reaction to give OH^- moieties in the solution.[40] Therefore, to eliminate the effect of UV rays, the CER on Fe-Tp (on an FTO surface) was performed outside the spectro-electrochemical cell and a similar change in color was observed, as shown in Movie S2, suggestive of a mechanism consisting of an inherent change in the ligand structure. Moreover, the reversibility of this color change was tested by applying −1.0 V, and the red color started to appear again due to the reversible reduction of the C═O present in the ligand (Fig. S22).

In situ monitoring of local pH

It is crucial to note that the applied potential has an immense effect on the electrolyte, which further affects the reaction kinetics. Thus, a change in local pH during the chlorine evolution reaction is inevitable according to eqn (8), yet it remains unexplored.

$$2HCl \rightleftarrows 2H^+ + Cl_2 \quad (8)$$

eqn (8) suggests that more protons are produced during the CER, consistent with the deprotonation of water molecules discussed in the above section. Therefore, the changes in the local pH were evaluated using four-electrode microelectrochemical analysis using a gold (Au) microelectrode

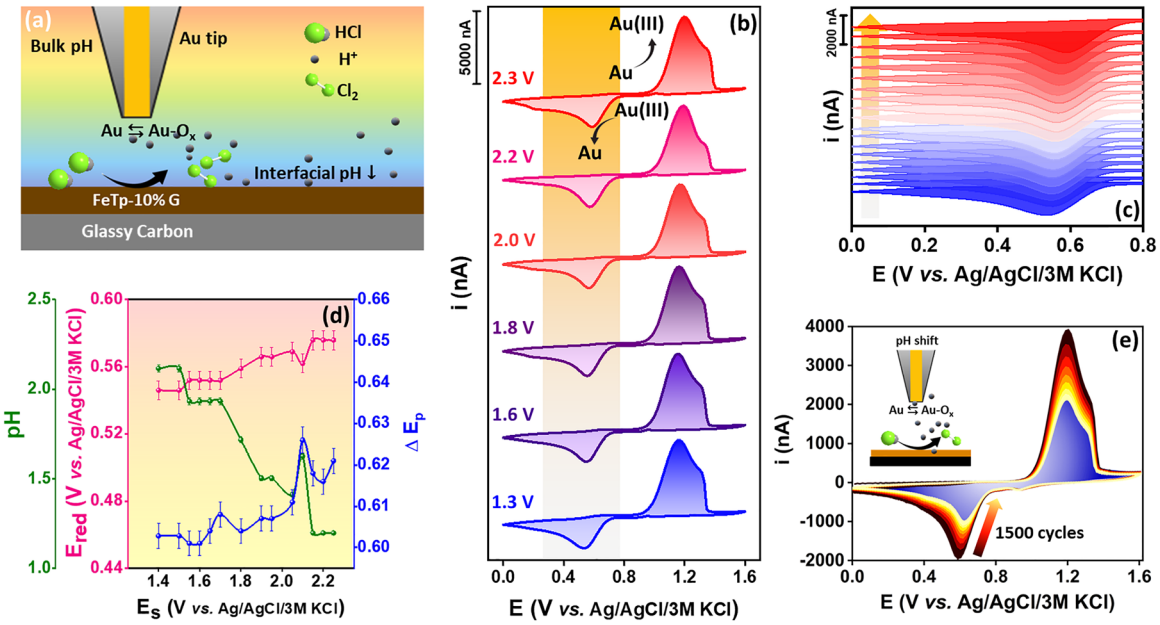

Fig. 3 (a) Schematic representation of the microelectrode studies of the local pH changes, (b) CV curves for the Au microelectrode (WE1, Ø = 100 μm) at different substrate (WE2) potentials, (c) corresponding enlarged part of the CV curves showing a shift in the reduction peak potential when WE2 was subjected to different potentials, (d) change in pH, E_{red} and peak potential difference extracted from figure (b) and (e) 1500 CV cycling curves recorded for the Au microelectrode when WE2 was simultaneously polarized at 1.9 V.

(tip, Ø = 100 μm) as working electrode 1 (WE1), a Fe-Tp-10% G catalyst-coated glassy carbon plate (GCE) as working electrode 2 (WE2), and Ag/AgCl/3 M KCl and a graphite rod as the reference and counter electrodes, respectively (Fig. 3a).

Initially, CV was conducted at the Au tip in the potential range of 0 V to 1.6 V *vs.* Ag/AgCl/3 M KCl in different electrolytes with varying pH (~12 to ~0). A pair of redox peaks corresponding to Au/AuO_x was observed and as the pH is decreased, there is a significant anodic shift in the reduction peak (Fig. S23a). Subsequently, a calibration curve of pH *vs.* E_{red} was drawn (Fig. S23b).[18,41] Thereafter, the WE2 was polarized at increasing anodic potentials ranging from 1.3 V to 2.3 V, and simultaneously, CV was conducted at WE1 in sample generation-tip collection (SG-TC) mode (Fig. 3b, c and Fig. S24). As observed from Fig. 3b and c, as the sample was polarized to more anodic potentials, the peak potential corresponding to the reduction (E_{red}) of AuO_x shifted to become more positive and thus, a decrease in pH was observed (Fig. 3d, according to eqn (8)), which is supported by the calibration curve. Strikingly, a similar change in pH was also observed with time when the sample (WE2) was polarized at a fixed potential of 1.9 V, and a total of 1500 CV cycles (Fig. 3e) were recorded at WE1 concurrently (~2.5 h). The decrease in local pH causes the shift in the AuO_x reduction peak;[42] however, repeated cycling induces surface roughening on the Au microelectrode, reducing the active sites and causing the cathodic peak current decay.[43] The monitoring of local pH allows for a qualitative analysis of reaction kinetics using the peak potential difference (ΔE_p). It could be observed that an increase in ΔE_p indicates slower electron transfer at higher substrate potentials.

Computational studies

Density-functional theory (DFT) calculations were performed to gain mechanistic insights into the CER and to rationalize the catalytic performance of the graphene, Fe-Tp MOF, and Fe-Tp-G systems using the Vienna *Ab initio* Simulation Package (VASP).[44–46] The detailed computational methodology is provided in the SI. The structural models of graphene, Fe-Tp MOF, and Fe-Tp-G are illustrated in Fig. 4a–c.

To reduce the computational cost while preserving the essential structural characteristics of the framework, a single molecular unit of the Fe-Tp MOF was modeled (Fig. 4b) and employed for subsequent calculations. To investigate the CER activity in acidic media on graphene, the Fe-Tp MOF, and Fe-Tp-G systems, a two-electron transfer reaction mechanism was examined through two possible pathways involving Cl* and OCl* intermediates (* denotes an adsorbed species).[47] The most stable adsorption sites, the Fe center in the Fe-Tp MOF and the C site in graphene, were considered for the construction of the free-energy profiles of the reaction. The corresponding adsorption energies for each intermediate are provided in Table S5 (detailed in the SI). Fig. 4d–f illustrates the Gibbs free-energy change (ΔG) associated with each intermediate step involved in the reaction step. The two plausible mechanistic pathways were investigated, and the computed ΔG values of the elementary steps for the CER are provided in the SI (Table S6). At an equilibrium potential of 1.36 V, the reaction pathway proceeding through the *OCl intermediate exhibits a potential-determining step with an overpotential (η) exceeding 2 V for all the systems considered, indicating that this pathway

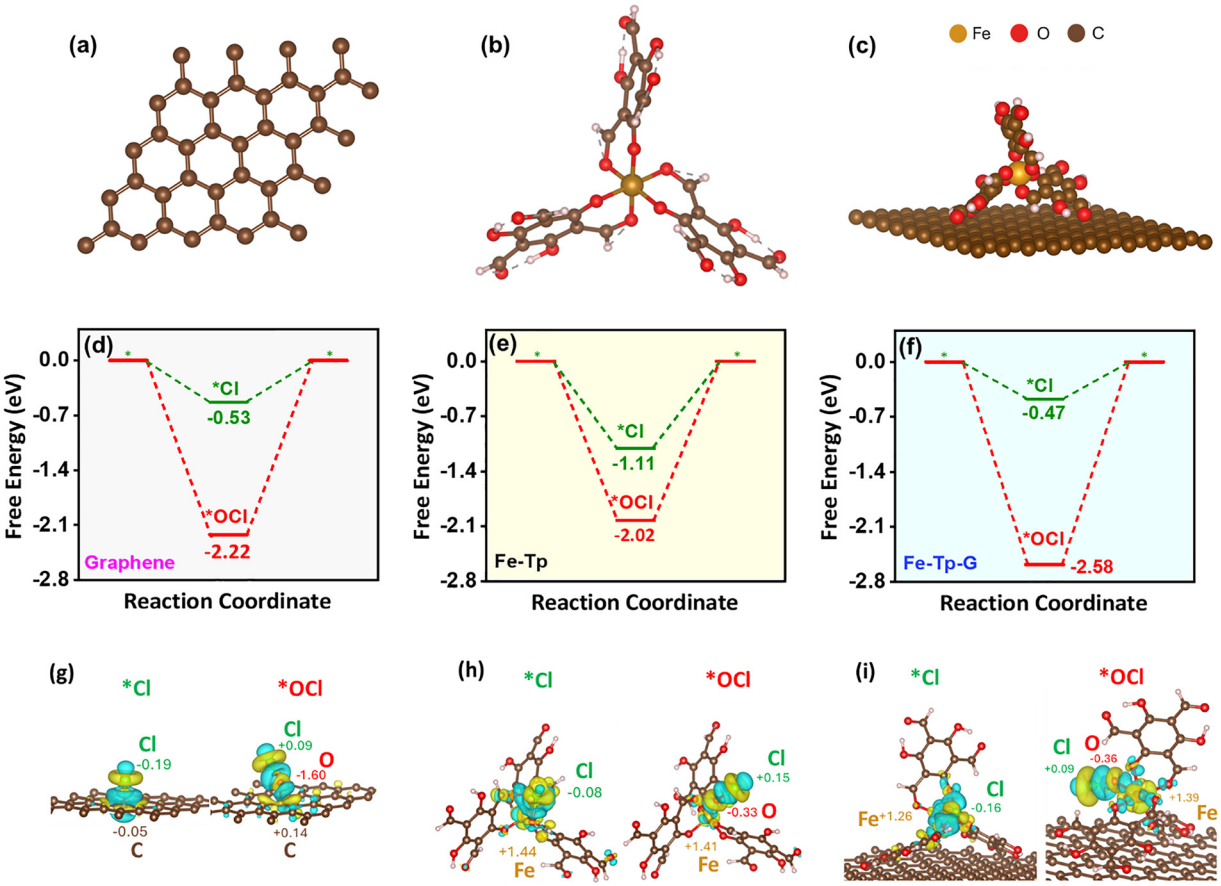

Fig. 4 Theoretical understanding of the CER mechanism: optimized structures of (a) graphene, (b) Fe-Tp MOF and (c) Fe-Tp-G; reaction free-energy profiles for CER in acidic medium at U = 1.36 V on (d) graphene, (e) Fe-Tp MOF, and (f) Fe-Tp-G, derived from the most stable adsorption sites for the OCl* and Cl* intermediates; (g)–(i) charge density difference (CDD) plots of electron redistribution during *Cl and *OCl adsorption on the three catalysts (isosurface = 0.003 e Å^{-3}), along with the corresponding Bader charge transfer values, highlighting the interfacial electronic interactions governing catalytic activity.

is thermodynamically unfavourable. In contrast, the pathway involving the *Cl intermediate demonstrates a significantly reduced overpotential, indicating a more favourable reaction route. Notably, the Fe-Tp-G system exhibits the highest catalytic activity, characterized by the lowest overpotential of −0.47 V. These DFT-derived results are in good agreement with the experimental observations, thereby further confirming that the Fe–Tp-G framework provides a more efficient catalytic platform for the CER.

To elucidate the catalytic activity, adsorption energies, Bader charge analysis, and charge density difference (CDD) calculations were performed. The results indicate that the *Cl pathway is more favourable than the *OCl pathway due to more optimal adsorption energies (Table S6). For *Cl adsorption, pristine graphene shows stronger interaction than Fe-Tp-G, accompanied by a more negative charge on *Cl, as evidenced by the Bader charge and CDD analyses (Fig. 4g–i). In contrast, the molecular Fe-Tp unit exhibits the strongest adsorption and charge transfer for *OCl due to the more positively charged Fe center. Fe-Tp-G, however, provides moderated adsorption with balanced charge transfer, which favors the *Cl pathway and enhances CER activity. The CDD plots further corroborate these findings.

Electrochemical oxygen reduction reaction

To ensure the successful bifunctional behavior of the designed catalyst for its utilization in a Zn-HCl/ORR battery, the electrochemical ORR activities of Fe-Tp and Fe-Tp-10% G were assessed by recording the LSV curves in O_2-saturated 0.4 M HCl electrolyte from 0.6 V to −0.1 V on a rotating ring-disk electrode (RRDE) at a rotation rate of 1300 rpm and a scan rate of 5 mV s^{-1}. Interestingly, Fe-Tp-10% G exhibited a superior performance in the ORR (Fig. 5a) with an onset potential of 0.3 V at −1 mA cm^{-2} and reached a higher diffusion-limiting current density of −2.7 mA cm^{-2} at −0.1 V, as compared to only Fe-Tp (−1.61 mA cm^{-2}). The superior activity of Fe-Tp-10% G could be ascribed to increased conductivity of the electrocatalyst and the presence of π–π interactions of graphene with the O_2 molecules, increasing its adsorption and simultaneously, weakening the O-O bonding for efficient ORR.[48–50]

Furthermore, the ORR performances were evaluated at different rotation rates (0 to 1300 rpm) to evaluate the kinetics

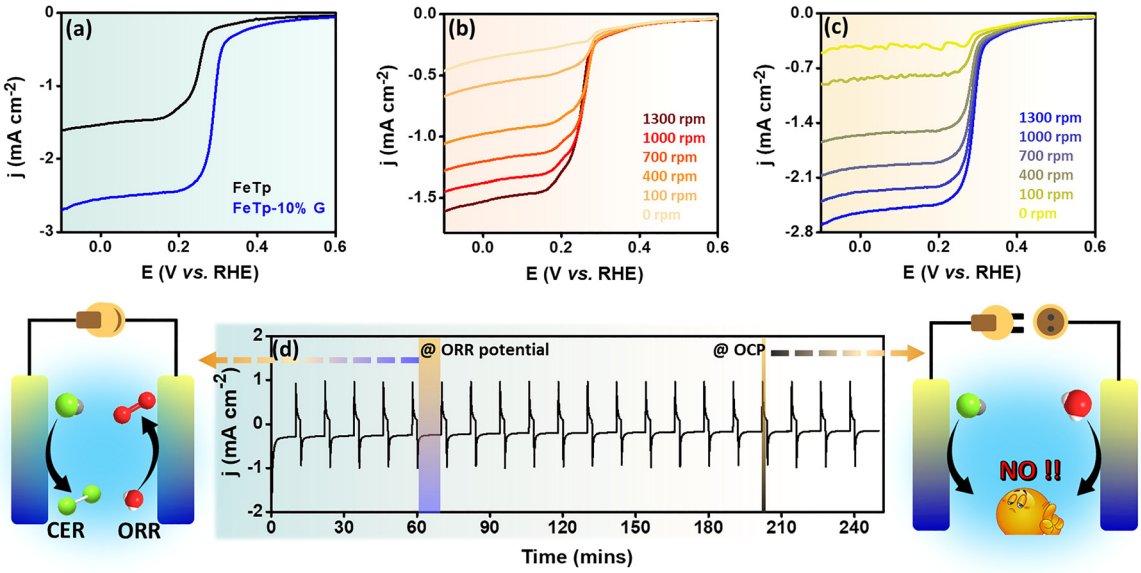

Fig. 5 (a) Polarization curves for Fe-Tp and Fe-Tp-10% G in O_2 saturated 0.4 M HCl at a scan rate of 5 mV s^{-1} and a rotation rate of 1300 rpm, RRDE polarization curves of (b) Fe-Tp and (c) Fe-Tp-10% G in O_2 saturated 0.4 M HCl electrolyte at various rotation rates, and (d) chronoamperometric analysis performed for 10 minutes of operation at 0.0 V and 2 minutes of shutdown (*i.e.* system off) for the Fe-Tp-10% G catalyst along with a schematic representation of the reaction mechanism.

of the reaction (Fig. 5b and c). As expected, the current density increased with an increase in rotation rates for both the catalysts. Afterwards, Koutecký–Levich (K–L) analysis was carried out from the disc polarization curves of the RRDE to determine the kinetic parameters and the number of electrons involved in the ORR for all catalysts. The K–L plots illustrate linear behavior between the inverse of the current density (j^{-1}) and the square root of the inverse of the rotation rate ($\omega^{-1/2}$) at 0.05 V, 0 V, −0.05 and −0.10 V *vs.* RHE, demonstrating first-order kinetics (Fig. S25a and b). Also, the number of electrons was found to be ∼2–3 for both catalysts at all potentials, demonstrating a 2 + 2e^- reaction pathway for the ORR. Also, the ring current (details in the SI) measurement was employed to quantify the amount of H_2O_2 formed during the ORR in 0.4 M HCl (Fig. S26). Fig. S27 shows a maximum H_2O_2 percentage of 22% with a F.E. of 23% at 0.45 V, showing a decrease with an increase in the reduction potential. Further, the ORR activity of Fe-Tp-10% G was compared with the HER (hydrogen evolution reaction) activity in O_2-free conditions (Ar-saturated electrolyte), and a significant decrease in the current density (from −0.5 mA cm^{-2} to −0.22 mA cm^{-2} at −0.2 V) was observed and no faradaic reaction was seen till −0.05 V (Fig. S28). To understand the applicability of Fe-Tp-10% G for industrial applications, stability studies were performed by mimicking industrial conditions *i.e.*, under sudden shutdown conditions during the ORR.

Therefore, 20 cycles and 200 cycles of chronoamperometric experiments were performed in O_2-saturated 0.4 M HCl electrolyte by polarizing the sample at 0.1 V for 10 min, followed by shutdown at open circuit potential (OCP, *i.e.*, at 0 V *vs.* E_{oc}) for 2 min, and the current was recorded. As observed from Fig. 5d, the stable current response seen even after 20 cycles (4 h) and 200 cycles (40 h, Fig. S29) under multiple shutdowns endorsed the high stability of the catalyst. Subsequently, the catalyst was subjected to XPS, FE-SEM, P-XRD and HR-TEM analysis to understand any changes following prolonged CER and ORR processes. As shown in Fig. S30a, the Fe2p XPS spectra show the conversion of Fe^{3+} to Fe^{2+} upon the application of the ORR potential, as depicted by the increase in the area of the Fe^{2+} peak (at a higher binding energy) relative to that of the Fe^{3+} (at lower binding energy). Whereas, after the CER, the Fe^{2+} peak disappeared, which is evidently due to the application of an oxidative potential (Fig. S31a). However, no significant changes were observed in the C1s and O1s XPS spectra (Fig. S30 and S31). Also, the P-XRD spectra (Fig. S32), FE-SEM (Fig. S33) and HRTEM (Fig. S34) analyses after the CER suggested the structure of Fe-Tp-10% G remains intact with nearly the same mass fraction of Fe present, as shown by the TEM-EDS spectra (Table S7). The presence of Cl in the TEM-EDS dot mapping is from the HCl electrolyte.

Scanning electrochemical microscopy studies of the local electrocatalytic activity

To understand the local electrocatalytic activity of the catalysts during the ORR and their stability in corrosive HCl media, the redox competition scanning electrochemical microscopy (RC-SECM) mode (detailed in the SI) was performed using array-scan measurements along the *x*–*y* plane.[18,27,29,30,32,33,51–56] We utilized an Au microelectrode (Ø = 100 μm) as working electrode 1 (WE1), the catalyst (Fe-Tp and Fe-Tp-10% G) drop-casted on a glassy carbon (GC) plate as WE2, Pt wire as the CE and Ag/AgCl/3 M KCl as the RE. A potential pulse profile was applied to the Au tip (WE1), wherein a base potential of 0.8 V was applied for 5 ms where no reaction takes place followed by application of the ORR potential (0 V) for 5 s and then again followed by the base

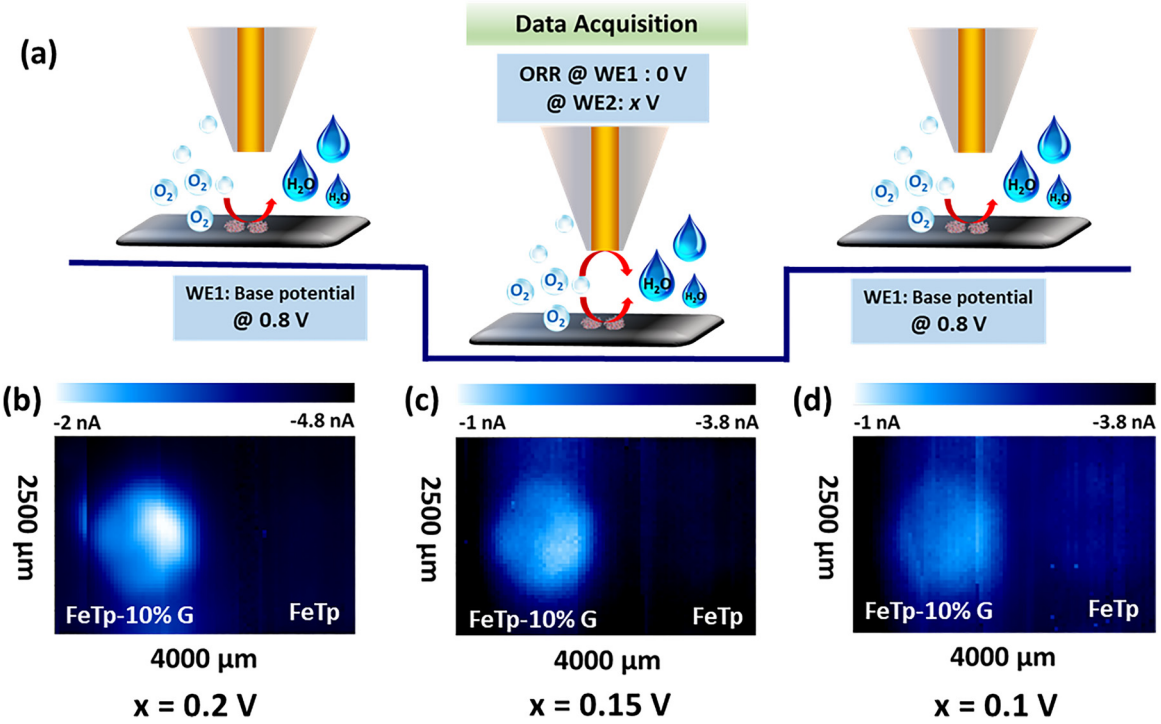

Fig. 6 (a) Schematic representation of the pulse profile used for the ORR in 0.4 M HCl. 2D RC-SECM images for the ORR over Fe-Tp-10% G and Fe-Tp at WE2 potentials of (b) 0.2 V, (c) 0.15 V, and (d) 0.1 V where WE 1 was constantly subjected to the pulse profile in (a).

potential. On the other hand, the sample (WE2) was polarized at different ORR potentials (Fig. 6a).

The 2D SECM images shown in Fig. 6b–d clearly show a good color contrast between the active catalyst Fe-Tp and Fe-Tp-10% G areas and the unmodified region (GC), which is attributed to the availability of O_2 in the gap between the tip and the sample. As the Au tip passes over the active catalyst zone where the electrolyte was depleted of oxygen (due to reduction of O_2 by the catalyst) a lower current was observed at the tip, while a higher tip current was observed over the zones rich in oxygen. The image colors change from navy blue through light blue to white; the white colour indicates a smaller tip current and hence high ORR activity of the Fe-Tp-10% G in HCl media. For better visibility of the notable changes in the local electrocatalytic activity between the two Fe-Tp-10% G and Fe-Tp catalysts, both the 2D and 3D SECM images are presented at different scales (Fig. S35). More importantly, the ORR activity changes with the applied sample potential, indicating that the observed behavior is due to the activity of the catalyst and not due to the topography. This superior bifunctional activity of Fe-Tp-10% G over Fe-Tp could be credited to the facilitated charge transfer at the electrode–electrolyte interface due to the presence of graphene. This is corroborated by the lower charge transfer resistance (R_{ct}) obtained from the electrochemical impedance spectroscopy (EIS, Fig. S36) studies, which is further supported by the higher electrochemically active surface area (ECSA, Fig. S37, detailed in the SI).

Zn-ORR/CER battery performance

The exceptional bifunctional activity of Fe-Tp-10% G towards the CER and ORR inspired us to assemble a Zn-ORR/CER battery. The battery was assembled using a home-made H-type cell from a cathode consisting of the catalyst coated on carbon paper placed in 0.4 M HCl electrolyte, an anode made from Zn foil in 1 M KOH + 0.02 M $Zn(OAc)_2$ electrolyte, and a membrane separator. The rechargeable Zn-ORR/CER battery involves $4e^-$ oxygen reduction producing H_2O during discharge, followed by spontaneous formation of zincate anions ($Zn(OH)_4^{2-}$). During charging, the CER (Cl_2 production) occurs, coupled with Zn deposition at the anode (Fig. 7a). Notably, the choice of alkaline media over acidic media at the anodic side is crucial, as Zn reacts aggressively in acidic media and is prone to corrosion. The assembled battery was subjected to open circuit voltage (OCV) and a stable OCV of ~1.60 V (Fig. S38) was recorded for 20 h and, as a practical demonstration, the cell was able to glow a red LED light of 1.5 V.

Afterwards, the linear polarization discharge curves for both the Fe-Tp and Fe-Tp-10% G catalysts in O_2-saturated 0.4 M HCl were compared from 1.5 V to 0.6 V *vs.* Zn/Zn^{2+}, and it was observed that similar to the half-cell studies, Fe-Tp-10% G exhibited a superior ORR activity (Fig. S39) as compared to Fe-Tp. As a control experiment, the discharge polarization curve for Fe-Tp-10% G was also recorded in Ar-saturated 0.4 M HCl. As shown in Fig. S40, the current density starts to decrease at a cell voltage of 1.32 V and the maximum power density of the assembled cell was calculated to be 5.4 mW cm^{-2} at a discharge current density of 8.46 mA cm^{-2} (Fig. S41a and b). In conjunction with the discharge, the charging reaction, *i.e.*, the CER, was evaluated by recording the LSV from 1.5 V to 3.0 V. An onset for the CER was observed at around 2.5 V (Fig. S41c), whereas upon replacing the HCl electrolyte with 0.2 M H_2SO_4, the oxidation

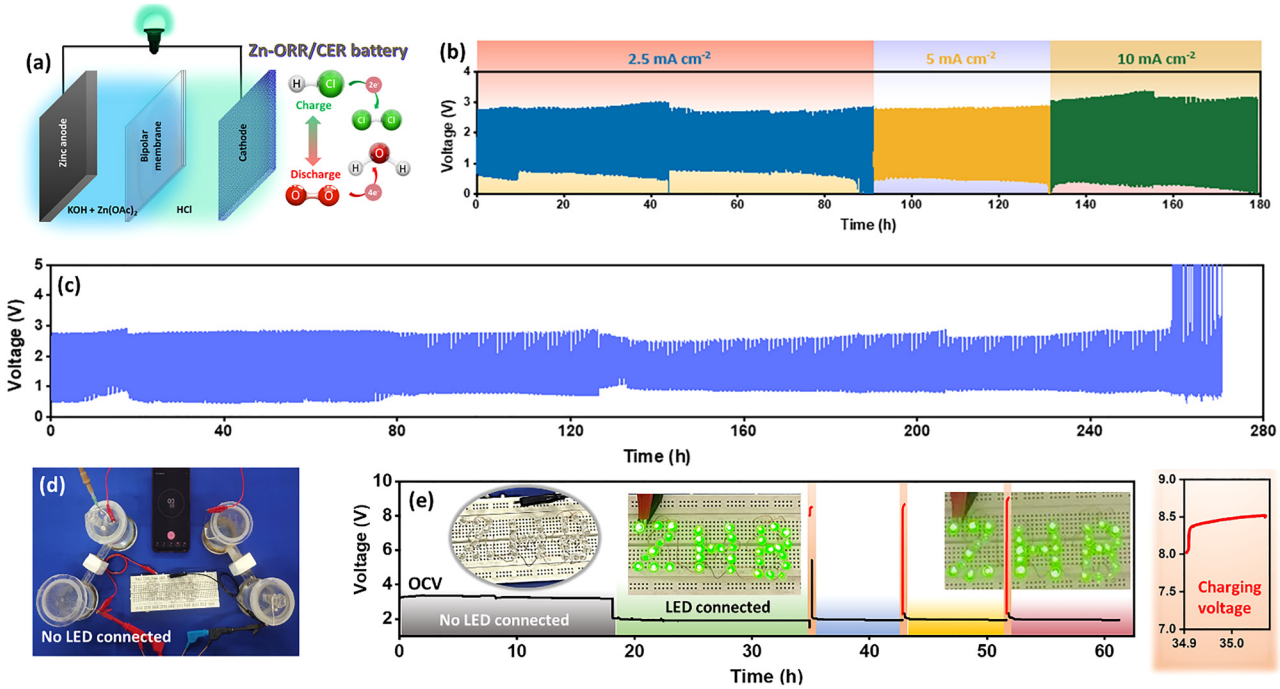

Fig. 7 (a) Schematic representation of the Zn-ORR/CER battery, (b) galvanostatic charge–discharge measurements at different current densities, (c) galvanostatic charge–discharge measurements at 2.5 mA cm^{-2}, (d) photographic image showing two cells connected in series but no load connected, and (e) voltage measurement during the practical demonstration of the battery; inset photographs showing 35 LEDs glowing while connected to the batteries at different time intervals.

current due to the OER started increasing after 2.8 V (Fig. S41c). It was also observed that Fe-Tp-10% G showed a better charge performance as compared to other variants (Fig. S41d). Therefore, for a rechargeable Zn-ORR/CER battery, the ORR and CER are involved as discharging and charging reactions. Moreover, sequential chronopotentiometry was recorded for both the discharge and charging processes at different current densities for 15 min each and a stable response at all current densities was observed when increasing from 0.5 mA cm^{-2} to 10 mA cm^{-2} and when applying reverse current density, thereby demonstrating stable battery performance (Fig. S42).

Further, the long-term stability of the battery was tested by recording galvanostatic charge–discharge at different current densities (2.5, 5, and 10 mA cm^{-2}, denoted as x mA cm^{-2}), where a discharge current of $-x$ mA cm^{-2} was applied for 10 min, followed by a charge current of $+x$ mA cm^{-2} for 10 min. It was observed that the battery was quite stable and after some time, the Zn anode was polished to be operated again at a different current density (Fig. 7b). The battery showed an energy density of 804 Wh kg^{-1} when discharged at 5 mA cm^{-2} (Fig. S43). Also, as the battery setup comprises two widely different pH levels in both chambers of the H-cell, a bipolar membrane could prove to be viable for the Zn-ORR/CER battery. Therefore, we compared the galvanostatic charge–discharge cycling stability using both a proton exchange and a bipolar membrane (BPM, detailed in the SI). It was observed that at a current density of 2.5 mA cm^{-2}, the BPM illustrated an enhanced cycling stability of >250 h (Fig. 7c and Fig. S44). This long-term stability test *via* galvanostatic charge–discharge experiments was carried out in the presence of O_2 gas. As O_2 dissolves in the electrolyte (0.4 M HCl), the discharge voltage starts increasing, resulting in a reduced voltage gap that indicates the discharge reaction is the ORR. However, the O_2 was cut-off after sufficient dissolution, but as the reactant gas gets consumed during discharge, the voltage gap starts to increase. Thus, the fluctuation in the voltage gap during the stability tests is attributed to the above phenomenon.

Another advantage of this battery system is its use in practical applications. For this purpose, two Zn-ORR/CER batteries were connected in series (Fig. 7d) and an OCV of $\sim$3.4 V was observed (Fig. 7e). After about 18 h, the cells were connected to an LED panel of 35 green LEDs (1.9 V) connected in parallel and the LEDs glowed for about 16 h (Fig. 7e and Fig. S45). Afterwards, the cells were charged for 10 min at 10 mA, which led to a successful and continuous discharge for about 8 h. This cycle was repeated 2 times, and similar behaviour was observed. The above findings demonstrate that this field could prove to be of new interest and create pathways to produce Cl_2 along with simultaneous energy storage.

Conclusions

This work presents a sustainable Zn-ORR/CER battery that not only enables green Cl_2 production as an industrially valuable product from important industrial HCl waste but also addresses energy storage demands through a "*three targets, one shot*" approach. The use of an iron-based MOF as a

bifunctional catalyst ensures robustness under harsh conditions, while mechanistic insights from DFT studies elucidate the CER pathway and associated local pH dynamics. Demonstrating rapid charging and reliable energy delivery, this system highlights a promising platform for integrating chemical production with energy storage in future circular electrochemical technologies.

Conflicts of interest

There are no conflicts to declare.

Data availability

The data supporting this article have been included as a part of the supplementary information (SI). Supplementary information includes the experimental details of the measurements including materials required, catalyst synthesis, characterization methods and data, electrochemical methods and data, the control experiments to compliment the results given in the manuscript, comparison tables and details for computational analysis. See DOI: https://doi.org/10.1039/d6ee00064a.

Acknowledgements

The authors thank the Central Research Facility (CRF), IIT Ropar for FE-SEM, XPS and HRTEM facilities and the AvH foundation, Germany for the SECM facility. S. K. thanks the CSIR (09/1005(0029)/2020-EMR-1) for a fellowship. K. G. thanks the Prime Minister Research Fellowship (PMRF) for a fellowship. TCN thanks the Anusandhan National Research Foundation (ANRF/PAIR/2025/000006/PAIR-A) for financial support. D. S. acknowledges the financial support from the Khalifa University Competitive Internal Research Award (CIRA-2021) and resource support under the Center for Catalysis and Separations (CeCaS). S. G. acknowledges Khalifa University for the PhD fellowship. A. K. M acknowledges Khalifa University for the research support. The authors acknowledge Dr Felipe Gandara (Instituto de Ciencia de Materiales de Madrid-CSIC, C/Sor Juana Inés de la Cruz 3, 28049 Madrid, Spain) for theoretical modelling of the material in the original article. H. M. acknowledges the Prime Minister's Research Fellowship (PMRF) for the research fellowship, and IIT Indore for lab and computational facilities.

References

1 Y. Liu, Y. An, J. Zhu, L. Zhu, X. Li, P. Gao, G. He and Q. Pang, *Nat. Commun.*, 2024, **15**, 977.
2 X. Liu, Y. Han, Y. Guo, X. Zhao, D. Pan, K. Li and Z. Wen, *Adv. Energy Sustainability Res.*, 2022, **3**, 2200005.
3 H. Chen, Z. Liu, H. Zhou, X. Yang and W. Lin, *Energy Environ. Sci.*, 2023, **16**, 5771–5791.
4 I. A. Moreno-Hernandez, B. S. Brunschwig and N. S. Lewis, *Energy Environ. Sci.*, 2019, **12**, 1241–1248.
5 Y. Zhao, S. Gu, K. Gong, J. Zheng, J. Wang and Y. Yan, *Angew. Chem., Int. Ed.*, 2017, **56**, 10735–10739.
6 M. Moser, C. Mondelli, A. P. Amrute, A. Tazawa, D. Teschner, M. E. Schuster, A. Klein-Hoffman, N. López, T. Schmidt and J. Pérez-Ramírez, *ACS Catal.*, 2013, **3**, 2813–2822.
7 R. Stringer and P. Johnston, *Chlorine and the environment: an overview of the chlorine industry*, 2001.
8 Centers for Disease Control and Prevention, 2020, https://www.cdc.gov/healthywater/drinking/public/water_disinfection.html? CDC_AA_refVal = https%3A%2F%2FError! Hyperlink reference not valid.
9 T. I. Partners, *GlobeNewsWire*, 2023.
10 J. Pérez-Ramírez, C. Mondelli, T. Schmidt, O. F. K. Schlüter, A. Wolf, L. Mleczko and T. Dreier, *Energy Environ. Sci.*, 2011, **4**, 4786–4799.
11 A. Goryachev, M. Etzi Coller Pascuzzi, F. Carlà, T. Weber, H. Over, E. J. M. Hensen and J. P. Hofmann, *Electrochim. Acta*, 2020, **336**, 135713.
12 R. K. B. Karlsson and A. Cornell, *Chem. Rev.*, 2016, **116**, 2982–3028.
13 L.-N. Zhang, R. Li, H.-Y. Zang, H.-Q. Tan, Z.-H. Kang, Y.-H. Wang and Y.-G. Li, *Energy Environ. Sci.*, 2021, **14**, 6191–6210.
14 T. C. Nagaiah, D. Gupta, S. D. Adhikary, A. Kafle and D. Mandal, *J. Mater. Chem. A*, 2021, **9**, 9228–9237.
15 A. Kafle, D. Gupta, S. Mehta, K. Garg and T. C. Nagaiah, *J. Mater. Chem. A*, 2024, **12**, 5626–5641.
16 I. Moussallem, J. Jörissen, U. Kunz, S. Pinnow and T. Turek, *J. Appl. Electrochem.*, 2008, **38**, 1177–1194.
17 D. Gupta, A. Kafle, P. P. Mohanty, T. Das, S. Chakraborty, R. Ahuja and T. C. Nagaiah, *J. Mater. Chem. A*, 2023, **11**, 12223–12235.
18 S. Mehta, S. Kaur, K. Garg, M. Singh and T. C. Nagaiah, *Angew. Chem., Int. Ed.*, 2025, e202505593.
19 N. Thakur, M. Kumar, D. Mandal and T. C. Nagaiah, *ACS Appl. Mater. Interfaces*, 2021, **13**, 52487–52497.
20 S. Mehta, S. Kaur, M. Singh, M. Kumar, K. Kumar, S. K. Meena and T. C. Nagaiah, *Adv. Energy Mater.*, 2024, **14**, 2401515.
21 S. Mehta, M. Singh, K. Garg, R. N. Mishra, K. Kumar, M. Moirangthem, S. K. Meena and T. C. Nagaiah, *Adv. Energy Mater.*, 2025, **38**, 2501214.
22 S. Kaur, M. Kumar, D. Gupta, P. P. Mohanty, T. Das, S. Chakraborty, R. Ahuja and T. C. Nagaiah, *Nano Energy*, 2023, **109**, 108242.
23 M. Kumar and T. C. Nagaiah, *J. Mater. Chem. A*, 2023, **11**, 18336–18348.
24 M. Kumar and T. C. Nagaiah, *J. Mater. Chem. A*, 2022, **10**, 4720–4730.
25 A. Kafle, D. Gupta, A. Bordoloi and T. C. Nagaiah, *Nanoscale*, 2022, **14**, 16590–16601.
26 C. Jin, W. Xia, T. C. Nagaiah, J. Guo, X. Chen, N. Li, M. Bron, W. Schuhmann and M. Muhler, *J. Mater. Chem.*, 2010, **20**, 736–742.
27 A. Maljusch, T. C. Nagaiah, S. Schwamborn, M. Bron and W. Schuhmann, *Anal. Chem.*, 2010, **82**, 1890–1896.

28 Z. Zhou, Y. Kong, H. Tan, Q. Huang, C. Wang, Z. Pei, H. Wang, Y. Liu, Y. Wang, S. Li, X. Liao, W. Yan and S. Zhao, *Adv. Mater.*, 2022, **34**, 2106541.
29 V. Singh and T. C. Nagaiah, *J. Mater. Chem. A*, 2019, **7**, 10019–10029.
30 V. Singh, S. D. Adhikary, A. Tiwari, D. Mandal and T. C. Nagaiah, *Chem. Mater.*, 2017, **29**, 4253–4264.
31 D. Gupta, A. Kafle, A. Chaturvedi and T. C. Nagaiah, *ChemElectroChem*, 2021, **8**, 2858–2866.
32 S. Kaur, K. C. Ranjeesh, K. Garg, S. Gaber, S. Mehta, T. C. Nagaiah and D. Shetty, *J. Mater. Chem. A*, 2024, **12**, 8516–8525.
33 S. Kaur, K. Garg and T. C. Nagaiah, *ACS Energy Lett.*, 2025, **10**, 1430–1438.
34 A. K. Mohammed, P. Pena-Sánchez, A. Pandikassala, S. Gaber, A. A. AlKhoori, T. Skorjanc, K. Polychronopoulou, S. Kurungot, F. Gándara and D. Shetty, *Chem. Commun.*, 2023, **59**, 2608–2611.
35 Y. Dai, Z. Xiong, H. Yin, C. Lai, X. Weng, Z. Chen and L. Shi, *J. Am. Chem. Soc.*, 2025, **147**, 39681–39692.
36 K. Liu, J. Fu, Y. Lin, T. Luo, G. Ni, H. Li, Z. Lin and M. Liu, *Nat. Commun.*, 2022, **13**, 2075.
37 C. Jing, H. Zhang, Q. Zhang, Z. Lu, L. Zhuo, S. Chen, Y. Qin, J. Luo and P. Jia, *Langmuir*, 2025, **41**, 33564–33574.
38 S. Gaber, A. K. Mohammed, B. H. Javaregowda, J. I. Martínez, P. P. Sánchez, F. Gándara, K. Krishnamoorthy and D. Shetty, *Angew. Chem., Int. Ed.*, 2024, **63**, e202409256.
39 A. Khayum Mohammed, A. Pandikassala, P. Pena Sánchez, S. Abdullah Gaber, S. Canossa, M. Kurian, G. Xavier, Y. He, F. Gándara, S. Kurungot and D. Shetty, *Chem. Eng. J.*, 2024, **496**, 153589.
40 J. Xiao, S. Guo, D. Wang and Q. An, *Chem. – Eur. J.*, 2024, **30**, e202304337.
41 L. Li, R. P. Antony, C. S. Santos, N. Limani, S. Dieckhöfer and W. Schuhmann, *Angew. Chem., Int. Ed.*, 2024, **63**, e202406543.
42 L. Li, N. Limani, R. P. Antony, S. Dieckhöfer, C. Santana Santos and W. Schuhmann, *Small Sci.*, 2024, **4**, 2300283.
43 A. R. Silva Olaya, B. Zandersons and G. Wittstock, *ChemElectroChem*, 2020, **7**, 3670–3678.
44 G. Kresse and D. Joubert, *Phys. Rev. B: Condens. Matter Mater. Phys.*, 1999, **59**, 1758–1775.
45 P. E. Blöchl, *Phys. Rev. B: Condens. Matter Mater. Phys.*, 1994, **50**, 17953–17979.
46 J. P. Perdew, K. Burke and M. Ernzerhof, *Phys. Rev. Lett.*, 1996, **77**, 3865–3868.
47 K. S. Exner, *Phys. Chem. Chem. Phys.*, 2020, **22**, 22451–22458.
48 P. Karthik, R. Vinoth, P. Zhang, W. Choi, E. Balaraman and B. Neppolian, *ACS Appl. Energy Mater.*, 2018, **1**, 1913–1923.
49 G. Kumar, S. K. Das, E. E. Siddharthan, A. Biswas, S. Bhardwaj, M. Das, R. Thapa and R. S. Dey, *J. Mater. Chem. A*, 2023, **11**, 18740–18754.
50 D. Higgins, P. Zamani, A. Yu and Z. Chen, *Energy Environ. Sci.*, 2016, **9**, 357–390.
51 T. C. Nagaiah, D. Schäfer, W. Schuhmann and N. Dimcheva, *Anal. Chem.*, 2013, **85**, 7897–7903.
52 A. Joshi, W. Schuhmann and T. C. Nagaiah, *Sens. Actuators, B*, 2016, **230**, 544–555.
53 A. Tiwari, V. Singh, D. Mandal and T. C. Nagaiah, *J. Mater. Chem. A*, 2017, **5**, 20014–20023.
54 S. Mehta, D. Gupta and T. C. Nagaiah, *ChemElectroChem*, 2022, **9**, e202101336.
55 D. Gupta, S. Chakraborty, R. G. Amorim, R. Ahuja and T. C. Nagaiah, *J. Mater. Chem. A*, 2021, **9**, 21291–21301.
56 S. Mehta, N. Elmerhi, S. Kaur, A. K. Mohammed, T. C. Nagaiah and D. Shetty, *Angew. Chem., Int. Ed.*, 2025, **64**, e202417403.

